Interaction-enhanced transmission imaging with Rydberg atoms

Xiaoguang Huo,[1] J. F. Chen,[2,3] Jing Qian,[1,*] and Weiping Zhang[4,5,6]

[1]*State Key Laboratory of Precision Spectroscopy, Department of Physics, School of Physics and Electronic Science, East China Normal University, Shanghai 200062, China*

[2]*Guangdong Provincial Key Laboratory of Quantum Science and Engineering, Southern University of Science and Technology, Shenzhen 518055, China*

[3]*Shenzhen Institute for Quantum Science and Engineering, Southern University of Science and Technology, Shenzhen 518055, China*

[4]*School of Physics and Astronomy and Tsung-Dao Lee Institute, Shanghai Jiao Tong University, Shanghai 200240, China*

[5]*Shanghai Research Center for Quantum Science, Shanghai 201315, China*

[6]*Collaborative Innovation Center of Extreme Optics, Shanxi Universty, Taiyuan, Shanxi 030006, China*

(Received 21 October 2020; revised 25 January 2021; accepted 10 January 2022; published 24 January 2022)

Atomic-scale imaging offers a reliable tool to directly measure the movement of microscopic particles. We present a scheme for achieving a nondestructive and ultrasensitive imaging of Rydberg atoms within an ensemble of cold probe atoms. This is made possible by the interaction-enhanced electromagnetically induced transparency at off resonance which enables an extremely narrow absorption dip for an enhanced transmission. Through the transmission of a probe beam, we obtain the distribution of Rydberg atoms with both high spatial resolution and fast response, which ensures a more precise real-time imaging. Increased resolution compared to the prior interaction-enhanced imaging technique allows us to accurately locate the atoms by adjusting the probe detuning only. This type of interaction-enhanced transmission imaging can be utilized in other impure systems containing strong many-body interactions, and is promising to develop superresolution microscopy of cold atoms.

DOI: 10.1103/PhysRevA.105.012817

I. INTRODUCTION

The demand for imaging individual Rydberg atoms with high spatial and temporal resolutions gave birth to the development of versatile optical imaging techniques. Earlier methods accessible for that purpose were based on, e.g., the field ionization imaging [1,2] or fluorescence imaging [3,4] of atoms uncovering both virtues. However, these detection methods are destructive and the atoms cannot be reused. For showing important applications in diverse areas, such as the quantum information processing [5] and the precision measurement [6], a nondestructive and high-efficiency detection of Rydberg states is imperative. Recently a superconducting microwave cavity has been used for efficient single-shot nondestructive measurement of Rydberg-atom ensembles enabled by its enhanced sensitivity [7], and a pulsed ion microscope was just reported for an achievable resolution below 200 nm [8]. These achievements open up new perspectives for imaging Rydberg atoms.

Alternatively, a promising approach proposed by Refs. [9,10], is the interaction-enhanced imaging (IEI) which manifests as a nondestructive and state-selective optical detection of strongly interacting impurities. Over the last decade IEI has been actively pursued by experimental devotion in versatile systems [11,12] as a new protocol for investigating the readout of the time-resolved dynamics of ions [13], molecules [14], or Rydberg qubits [15], the generation of a single-photon transistor with high gain [16], and various long-range interactions [17,18]. IEI underlyingly relies on the strong impurity-probe interaction in the vicinity of each impurity, which can induce an enhanced absorption imaging in the case of resonant electromagnetically induced transparency (EIT) [19,20]. EIT spectra enable a direct nondestructive detection of highly excited Rydberg levels [21]. And the interaction-induced Rydberg blockade has found wide applications in quantum information processing [22]. By mapping this strong Rydberg-Rydberg interaction onto the light field one can resolve the property of each impurity without destroying it. However, as for Rydberg impurities, their spatial response range is limited by the Rydberg blockade radius, typically around a few micrometers [23,24]. Reducing it down to the level of submicrometer scale has to involve a strong coupling laser, which is still challenging for current experimental implementation.

In the present work we develop the protocol of IEI by placing it in an off-resonant EIT environment [25], which benefits from a very narrow absorption dip instead of a broad absorption peak, consequently named as *interaction-enhanced transmission imaging* (IETI). This dip is caused by the compensation between a big probe-atom detuning at off resonance and the strong impurity (target) -probe interaction, whose width can be flexibly adjusted to be orders of magnitude narrower than a typical blockade radius of a few micrometers. By carrying out such an off-resonant measurement with respect to the probe atoms, it is feasible to obtain an ultraprecise imaging of random Rydberg targets with its spatial resolution increased by one order of magnitude as compared to the IEI technique, which is also accompanied by a fast optical response in the real-time detection. Increased resolution in IETI can facilitate

*jqian1982@gmail.com

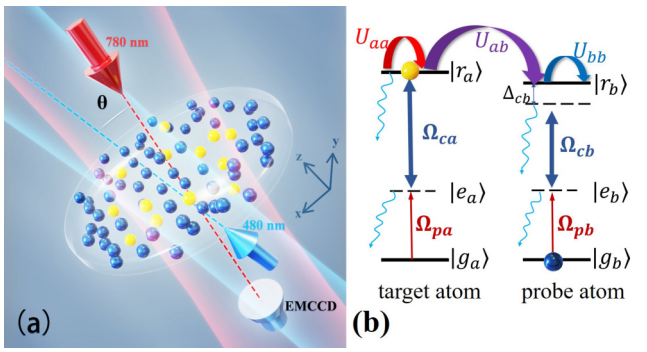

FIG. 1. (a) Sketch for the interaction-enhanced transmission imaging. Target atoms (yellow) are randomly embedded within an ensemble of dense quasi-two-dimensional probe atoms (blue) in the x-y plane. The probe atoms interact with two light fields (probe and coupling) propagating in the $-z$ and $+z$ directions, respectively, which are illuminated via a two-photon transition from the ground state $|g_b\rangle = |5S_{1/2}\rangle$ to the Rydberg state $|r_b\rangle = |80S_{1/2}\rangle$. The preparation of the Rydberg state $|r_a\rangle = |85S_{1/2}\rangle$ of target atoms is also enabled by a two-photon excitation. The probe and coupling lasers with wavelengths 780 and 480 nm, can induce a negligible Doppler shift as they are almost vertical to the stochastic atomic movements in the x-y plane. By detecting the probe-field transmission at the end of the $-z$ axis with a cooled EMCCD camera, the position of all target atoms could be precisely resolved from the formation of a narrow transmission ring. In order to reduce the scattering of the coupling laser, a tiny separation angle $\theta \leqslant 5^\circ$ between the probe and coupling beams is designed. (b) Relevant energy levels and atom-field interactions. The strong probe-target interactions U_{ab} will overcome the big detuning Δ_{cb} with respect to state $|r_b\rangle$, giving rise to an enhanced transmission rate at a specific probe-target spacing. U_{aa} and U_{bb} reflect the strength of target-target interactions and probe-probe interactions.

an accurate and quick positioning of atoms, especially when multi-Rydberg atoms overlap within a specific region. The scheme is deserving of future experimental exploration for the realization of superresolution microscopy of cold atomic ensembles.

II. THEORETICAL STRATEGY

The principle of our approach illustrated in Fig. 1 presents that a few target atoms surrounded by a large number of background probe atoms are randomly embedded in a quasi-two-dimensional system. Initially, given the ground target atoms, the probe atoms coupled by light fields Ω_{pb} and Ω_{cb} will suffer from an inefficient excitation due to the presence of a large off-resonant detuning $\Delta_{cb} \gg \Omega_{pb}, \Omega_{cb}$ with respect to $|r_b\rangle$. However, once the target atoms are excited to the Rydberg state $|r_a\rangle$ through a two-photon optical pumping with Rabi frequencies Ω_{pa} and Ω_{ca}, the induced probe-target interaction U_{ab} acts as an effective detuning for the detuned level $|r_b\rangle$. Here $U_{ab} = C_6^{ab}/R^6$ forms as a van der Waals (vdWs)–type for the S-S state interaction between two Rydberg levels, where C_6^{ab} is the interaction coefficient and R reflects the probe-target distance [23]. The presence of U_{ab} possibly overcomes Δ_{cb} with respect to the probe atom, and hence gives rise to a spatial EIT effect [26]. Therefore the position of such randomly distributed target atoms can be spatially resolved by utilizing a very narrow EIT transmission window at off resonance [27].

To describe the probe-atom absorption that undergoes an off-resonant EIT excitation, the Hamiltonian describing a single *probe* atom is given by

$$\mathcal{H}_b = -\tfrac{1}{2}(\Omega_{pb}|e\rangle\langle g|_b + \Omega_{cb}|r\rangle\langle e|_b + \text{H.c.}) + \Delta'_{cb}|r\rangle\langle r|_b. \tag{1}$$

The presence of an excited target atom will cause a finite energy shift U_{ab} to state $|r_b\rangle$, which has been translated into an effective two-photon detuning of the probe atoms $\Delta'_{cb} = \Delta_{cb} + U_{ab}$. For probe atoms, a typical excitation probability is very small due to the off-resonant detuning Δ_{cb} as well as $\Omega_{pb} \ll \Omega_{cb}$, making the probe-probe interaction U_{bb} negligible. However, in the resonant case where Δ_{cb} has been overcome by U_{ab} at a certain distance, U_{bb} adding to the two-photon detuning Δ'_{cb} may become an important factor during measurement (Appendix B). On the other hand, the target-target interaction U_{aa} plays a role only if more than two target atoms are coupled to state $|r_a\rangle$ at the same time, and we will consider this effect in the study of many-atom imaging.

Here we begin with a detailed analysis for the case of a single target atom. The evolution of the density matrix ρ_b of the probe atom is governed by the master equation,

$$\dot{\rho}_b = -i[\mathcal{H}_b, \rho_b] + \mathcal{L}_b, \tag{2}$$

with the Liouville operator $\mathcal{L}_b$ expressed as [28]

$$\mathcal{L}_b = \begin{pmatrix} \Gamma_{eg}\rho_{b,ee} & -\frac{1}{2}\gamma_2\rho_{b,ge} & -\frac{1}{2}\gamma_3\rho_{b,gr} \\ -\frac{1}{2}\gamma_2\rho_{b,eg} & -\Gamma_{eg}\rho_{b,ee}+\Gamma_{re}\rho_{b,rr} & -\frac{1}{2}(\gamma_2+\gamma_3)\rho_{b,er} \\ -\frac{1}{2}\gamma_3\rho_{b,rg} & -\frac{1}{2}(\gamma_2+\gamma_3)\rho_{b,re} & -\Gamma_{re}\rho_{b,rr} \end{pmatrix},$$

where $\rho_{b,ij}$ stands for the matrix element and the subscript b represents the probe atom. Γ_{ij} is the rate of population decay from state $|i\rangle$ to state $|j\rangle$ $(i, j = g, e, r)$. $\gamma_2 = \gamma_e + \Gamma_{eg}$ and $\gamma_3 = \gamma_r + \Gamma_{re}$, where γ_e and γ_r refer to the dephasing rate due to the loss of coherence in the atomic elastic collisions and other dynamics, which are not associated with the population transfer [29].

By taking $\dot{\rho}_b = 0$ in Eq. (2) we obtain the stationary element $\rho_{b,eg}$ for describing the probe transition [30],

$$\rho_{b,eg}(r, v)dv = \frac{\Omega_{pb}[2\delta(r) - i\gamma_3]}{\Omega_{cb}^2 + i\gamma_2[2\delta(r) - i\gamma_3]}\mathcal{N}(v)dv, \tag{3}$$

under the assumptions of $\Omega_{pb} \ll \Omega_{cb}$, $\rho_{b,gg} \approx 1$, $\rho_{b,ee} \approx 0$, and $\rho_{b,rr} \approx 0$. Remarkably, in Eq. (3) the new denotation $\delta(r)$ is expressed as

$$\delta(r) = \Delta_{cb} - \frac{C_6^{ab}}{R^6} + U_{bb} - (\vec{k}_c + \vec{k}_p)\cdot\vec{v}, \tag{4}$$

where the probe-target spacing $R = |r - r_a|$ represents the effective two-photon detuning and r_a is the random location of a stationary target atom. For a moving target atom r_a is also time dependent [see Eq. (10)]. Accounting for the thermal motion of probe atoms that translates into a Doppler frequency shift to the atomic internal levels we phenomenologically introduce this effect where $\mathcal{N}(v)$ in Eq. (3) is the number density of ^{87}Rb probe atoms with velocity $\vec{v}_b$ and $\vec{k}_{c,p}$ is the wave vectors of the coupling or probe beam. $\mathcal{N}(v)$ takes the form of a

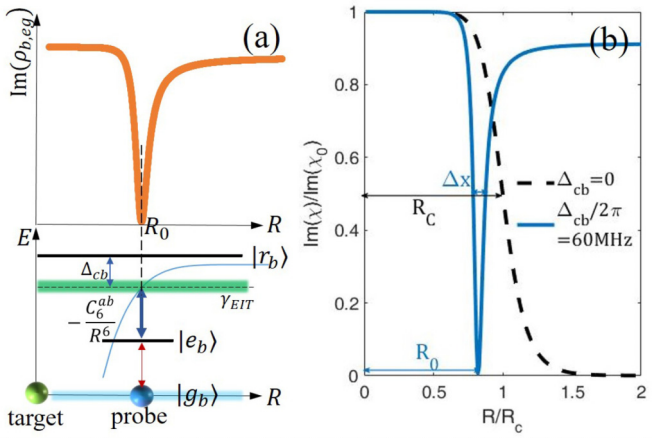

FIG. 2. (a) Imaginary part of $\rho_{b,eg}(r)$ represents the probe absorption. At a certain distance with $\delta(r) = 0$, it gives rise to a critical distance $R_0 \approx \sqrt[6]{C_6^{ab}/\Delta_{cb}}$ at which a narrow absorption dip emerges. (b) The absolute absorption Im$[\chi]$ normalized by $\mathrm{Im}(\chi_0) = 2n_0\mu_{eg}^2/(\epsilon_0\hbar\gamma_2)$ vs the relative spacing R (in units of $R_c = \sqrt[6]{2\gamma_2 C_6^{ab}/\Omega_{cb}^2}$) under various Δ_{cb} values. For $\Delta_{cb} = 0$ there exists a wider absorption-enhanced peak (black dashed line) within the Rydberg-blockade volume R_c, similar as in Fig. 2(b) of Ref. [10]. However, if $\Delta_{cb} \neq 0$ a narrower absorption dip (blue solid line) emerges, which ensures a strong transmission signal due to $\gamma_3 \ll \Omega_{cb}$. In plotting (b) we set $\Omega_{cb}/2\pi = 15\,\mathrm{MHz}$, $\Omega_{pb}/2\pi = 0.15\,\mathrm{MHz}$, $\gamma_2/2\pi = 6.1\,\mathrm{MHz}$, $\gamma_3/2\pi = 10\,\mathrm{kHz}$, and $C_6^{ab}/2\pi = 204.8\,\mathrm{GHz}\,\mu\mathrm{m}^6$.

Maxwell-Boltzmann function at thermal equilibrium. To reduce the impact of Doppler shift we design the two beams to propagate nearly vertical to the atom movement, as shown in Fig. 1(a). To this end, the susceptibility $\chi(r, v)$ corresponding to the atomic transition driven by the probe field is given by

$$\chi(r, v)dv = \frac{2\mu_{ge}}{\epsilon_0 E_p} n(r)\rho_{b,eg}(r, v)dv, \tag{5}$$

where the Gaussian atomic number density is $n(r) = n_0 \exp(-r^2/2\sigma_r^2)$ with n_0 the peak and σ_r the half-width. E_p is the probe electric field amplitude, μ_{ge} is the transition dipole moment, and ϵ_0 is the vacuum dielectric constant. The real (imaginary) part of the susceptibility $\chi(r, v)$ corresponds to the dispersion (absorption) of the probe light, caused by the atomic medium. By integrating the imaginary part of Eq. (5) over the velocity distribution for atomic temperature T_0 we can obtain an absolute absorption coefficient Im$[\chi(r)]$ as a function of R.

Figure 2 illustrates the probe absorption by calculating the imaginary part. First we understand the essence of transmission-enhanced imaging by following the map of Fig. 2(a). In the vicinity of an off-resonant driving probe atom, detuned by Δ_{cb} with respect to a Rydberg state $|r_b\rangle$, the energy level of $|r_b\rangle$ is also shifted by the strong probe-target potential $U_{ab} = C_6^{ab}/R^6$. Here $r_a = 0$ and $R = |r|$ are assumed. If satisfying $\Delta_{cb} - C_6^{ab}/R^6 \approx 0$ and $\Delta_{cb} \neq 0$ one can obtain a narrow absorption dip at $R_0 \approx \sqrt[6]{C_6^{ab}/\Delta_{cb}}$ with its width Δx much smaller than the blockade radius R_c. The strength of the Doppler shift $(\vec{k}_c + \vec{k}_p) \cdot \vec{v}_b$ can be made orders of magnitude smaller than the Rydberg shift U_{ab}. For example, a rough estimation based on the wave vector $|\vec{k}_c| = 13.09\,\mu\mathrm{m}^{-1}$ ($\lambda_c = 480$ nm), $|\vec{k}_p| = 8.06\ \mu\mathrm{m}^{-1}$ ($\lambda_p = 780$ nm), and the most probable speed $v_{\mathrm{mps}} = \sqrt{2kT_0/m} \approx 4.37$ cm/s at $T_0 = 10\,\mu$K, gives rise to a maximal value for describing the Doppler shift, which is $(|\vec{k}_c| + |\vec{k}_p|)v_{\mathrm{mps}} \approx 0.93\,\mathrm{MHz} \ll |U_{ab}|$. In fact, $\vec{k}_c$ and $\vec{k}_p$ are counterpropagating and almost vertical to the atomic velocity $\vec{v}_b$ in our scheme, leading to a perfect Doppler-free measurement. So $\delta(r) \approx \Delta_{cb} - C_6^{ab}/R^6$ is confirmed. Note that we also ignore the probe-probe interaction U_{bb} due to the poor probe excitation probability within the Rydberg EIT region for $\Omega_{pb} \ll \Omega_{cb}$. The influence of U_{bb}, especially at the position of absorption dip, has been explicitly discussed in Appendix B. The resulting enhanced probe transmission can precisely reflect the position of the target atom. This high-contrast and highly precise transmission signal could be suited for the target-atom imaging.

However, if $\Delta_{cb} = 0$ as in traditional IEI schemes, the absorption response manifests as an opposite change. As $R \to \infty$ the excited state $|r_b\rangle$ becomes resonant and suffers from a zero absorption. Yet within the blockade radius R_c, i.e., $R < R_c = \sqrt[6]{2\gamma_2 C_6^{ab}/\Omega_{cb}^2}$, an enhanced absorption can return a well signature for imaging the location of the target Rydberg atom, although the spatial resolution is relatively poor. Because the broad absorption which is restricted by R_c will make the position measurement insensitive. As a consequence, it is insufficient for achieving ultraprecise microscopic imaging of individual atoms by using traditional IEI technology.

A quantitative verification for different probe absorption rates is comparably illustrated in Fig. 2(b). It is clearly shown that the resonant case of $\Delta_{cb} = 0$ (black dotted) allows for an absorption-enhanced signal with its broad half-width R_c at half-maximum. However, our approach using $\Delta_{cb}/2\pi = 60\,\mathrm{MHz}$ (blue solid line) greatly benefits from a higher spatial resolution, characterized by an extremely narrow width Δx, which is given by

$$\Delta x \approx \left(\frac{C_6^{ab}}{\Delta_{cb} - \alpha}\right)^{1/6} - \left(\frac{C_6^{ab}}{\Delta_{cb} + \alpha}\right)^{1/6} \tag{6}$$

occurring at the absorption dip $R = R_0$ with $\alpha = \sqrt{\Omega_{cb}^4 - \gamma_2^2\gamma_3^2}/(2\gamma_2)$. At that place an approximately 100% transmission probability can be obtained. Δx is easily tunable by the detuning Δ_{cb}, and in principle $\Delta_{cb} \gg \alpha$ will lead to an arbitrary scale of spatial resolution because $\Delta x \to 0$ as long as the contrast of images permits. Such a narrower absorption dip could deeply improve the imaging precision for the target atoms, promising for the development of superresolution technology.

III. SINGLE-TARGET-ATOM IMAGING

A. High spatial resolution

To carry out numerical calculations for the EIT imaging of random-embedded target atoms, all the probe-target, probe-probe, and target-target interactions have to be considered. This is a many-body problem. In our calculation, to prepare multitarget atoms on Rydberg state we implement coherent population trapping (CPT) with respect to the target atoms

which were on the ground state initially [31]. The Rydberg excitation of target atoms will return a significant change to the EIT absorption signal of the surrounding probe atoms. The transmitted probe light on the surrounding probe atom serves for detection of target positions under the condition of off-resonant EIT.

In a practical experiment, given the ground atoms one has to prepare all target atoms onto their Rydberg states through repeated excitations in the CPT configuration. A numerical description for the multi-target-atom Rydberg preparation has been described in Appendix A. Here we simply consider the case of a single target atom at a stationary position r_a which was preprepared on the Rydberg state $|r_a\rangle$ before detection. The presence of such an excited target atom can modify $\delta(r)$ of the probe atoms, as defined in Eq. (4), returning an enhanced transmission signal for the probe light. It happens when $|r - r_a| = R_0$ is met. In the numerical simulation we assume $\{\rho_{a,rr}\} \equiv 1$ denoting its preexcitation. Denotations $\{\rho_{a,rr}\} \equiv 1$ and 0 means that the target atom is on $|r_a\rangle$ or not. Other parameters are as follows: a quasi-two-dimensional (quasi-2D) atomic ensemble with ultracold ^{87}Rb atoms at $T_0 = 10\ \mu$K, serves as the probe atoms. The peak probe atomic density is $n_0 = 5 \times 10^{11}\ \mathrm{cm}^{-3}$ and radially follows a Gaussian density distribution with a half-width $\sigma_r = 0.7$ mm [24]. The unique target atom placed in the center is also a rubidium atom. The specific experimental energy levels are $|g_b\rangle = |5S_{1/2}, F = 2, m_F = 2\rangle$, $|e_b\rangle = |5P_{3/2}, F = 3, m_F = 3\rangle$, and $|r_b\rangle = |80S_{1/2}\rangle$ for the probe atom; and $|r_a\rangle = |85S_{1/2}\rangle$ for the target atom. The vdWs coefficient is $C_6^{ab}/2\pi = 204.8\ \mathrm{GHz}\,\mu\mathrm{m}^3$ (calculated by [32]). Coefficients γ_2 and γ_3 are contributed by the decay rates of $|e_b\rangle$ and $|r_b\rangle$ and additional dephasing rates. The decay rates are estimated to be $\Gamma_{eg}/2\pi = 6.0$ MHz and $\Gamma_{re}/2\pi = 0.28$ kHz corresponding to energy levels [33]. The dephasing effect $\gamma_{e,r}$ comes from nonradiative collisions, Doppler shifts, inhomogeneous trapping potential, and the excitation laser linewidth [34]. The total damping rates are chosen to be $\gamma_2/2\pi = 6.1$ MHz and $\gamma_3/2\pi = 10$ kHz. To ignore the interaction between probe atoms, we require the maximal density on state $|r_b\rangle$ below 1.0 within the blockade radius of R_c', i.e., $\frac{\Omega_{pb}^2}{\Omega_{cb}^2} n L_z \pi R_c'^2 < 1.0$ [10]. Here $R_c' = 5.7\ \mu$m is for the probe-probe blockade. For realizing an EIT excitation the Rabi frequencies of the probe atom are chosen to be $\Omega_{pb}/2\pi = 0.15$ MHz and $\Omega_{cb}/2\pi = 15$ MHz.

With the above experimentally accessible parameters, we transform the absorption into the frame of probe transmission and obtain [35]

$$T(x, y) = |\exp\{ik_p L_z \chi(x, y)/2\}| \tag{7}$$

in order to show the transmission spectra where $k_p = |\vec{k}_p|$ is the probe wave vector and $L_z = 10\ \mu$m is the z-axis thickness of the medium. For realizing a quasi-2D system we use $L_z \ll L_{x,y}$. In plotting transmission T we reduce it into the form of

$$T = \exp[i\eta e^{-r^2/2\sigma_r^2} \rho_{b,eg}(x, y)] \tag{8}$$

with a dimensionless precoefficient $\eta = k_p L_z \mu_{ge} n_0/\epsilon_0 E_p \approx 29.19$ and $\mu_{ge} = 2.5 \times 10^{-29}$ C m.

As displayed in Figs. 3(a1) and 3(a2) the transmission signal of a single target atom is represented by one-cycle

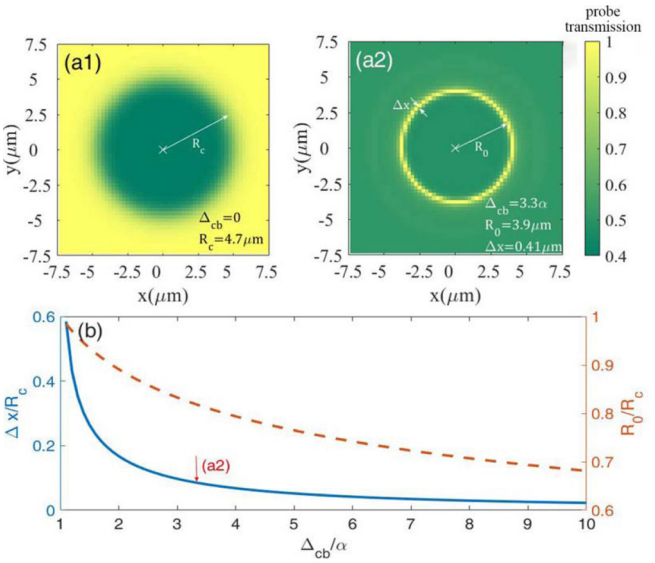

FIG. 3. Transmission images of a single target atom surrounded by a dense ensemble of probe atoms. The unique target atom is located at the center $x = y = 0$, denoted by a white cross. In (a1), by using $\Delta_{cb} = 0$ as in earlier IEI schemes, the spatial resolution R_c decided by the half-width of transmission, is smoothly increasing as $r = \sqrt{x^2 + y^2}$ grows; in contrast, (a2) shows a bright and narrow transmission ring at $r = R_0$ with $\Delta_{cb} = 3.3\alpha$, which serves as a more precise determination for the position of the target atom, because of its higher spatial resolution $\Delta x \approx R_c/10$. (b) The ratio $\Delta x/R_c$ (blue solid line) vs Δ_{cb} represents a significant decreasing tendency. The red dashed line shows that the ratio of R_0/R_c continuously decreases and is always smaller than 1.0 as Δ_{cb} increases. The red arrow points to the parameters used in (a2).

measurement within an amplified area of $(15 \times 15)\ \mu\mathrm{m}^2$. Each pixel is set to be a $(0.25\ \mu\mathrm{m})^2$ region to fit the width of the transmission ring. For $\Delta_{cb} = 0$ the location of the unique target atom denoted by a white cross, can be resolved in a broad disk area with its radius $R_c \approx 4.7\ \mu$m, which is equivalent to a typical blockade range. However, if a nonzero $\Delta_{cb}/2\pi = 60$ MHz is applied, as shown in (a2), one can easily envisage higher resolution given by an improved transmission signal with a spatial extent Δx smaller than R_c by one order of magnitude, by which a nondestructive detection for the central target atom is achievable. That fact is made possible by the exact compensation of the probe-target interaction U_{ab} for the off-resonant detuning Δ_{cb}. In the calculation we have also taken into account the probe-probe interaction U_{bb} as shown in Fig. 7(c), and it causes a bit poorer brightness as compared to the result shown in Fig. 3(a2). This is because Fig. 7(c) is obtained by averaging over 1000 stationary one-cycle measurements with random probe-atom excitations. If the probe-atom excitation is blocked by a big U_{bb} the target atom cannot be detected at this position, which lowers the ring brightness.

Therefore, our numerical results (Fig. 3) based on stationary one-cycle measurement of a preexcited target atom, show that both contrast and spatial resolution in the IETI approach are greatly improved if compared to the result of IEI with $\Delta_{cb} = 0$. Surely, a higher spatial resolution is principally satiable by a growing Δ_{cb}; however, the optical diffraction limit sets an obstacle to it which is not easy to overcome

without auxiliary techniques [36–38]. So in order to obtain an experimentally accessible image we will adopt the optimal parameters in Fig. 3(a2) for studying the many-atom case. In Fig. 3(b) we verify that the ratio $\Delta x/R_c$ characterizing the improved strength of the spatial resolution, can be made even smaller via an adjustment of Δ_{cb}. And at the same time the annulus radius R_0 in IETI can also be shrunk into much smaller than the blockade radius R_c as long as Δ_{cb} is appropriately chosen.

B. Fast response in real-time imaging

Nondestructive detection requires a repeated measurement for Rydberg targets; however, once the control or probe light switches with time, the detected system needs a finite response time for reaching a new equilibrium. This response speed of Rydberg EIT could qualify the property of the real-time imaging. So far a fast response property of Rydberg EIT has been verified to be facilitated by the presence of strong Rydberg-Rydberg interactions [39,40]. We numerically study the real-time absorption behavior of the probe atoms at a determined distance R_0 which could reflect the least time required for one-cycle measurement. The initial probe atoms are assumed to undergo a sudden switch on of the coupling light $\Omega_{cb}(t)$, consequently attaining a stationary state during the measurement time. But once the coupling laser is switched off after stable measurement $T_{\rm meas}$, the system tends to recover accompanied by a different recovering time. We can roughly estimate the least time required for a complete one-cycle measurement which should contain three processes of response, recover, and stationary measurement. A faster response time could improve the imaging quality, accelerating real-time detection in experiment.

Numerical results are obtained based on solving the time-dependent dynamics of $\mathrm{Im}(\rho_{b,eg})$ from the single-atom master equation (2) without the probe-probe interactions. We switch on the probe field Ω_{pb} at $t=0$ and preserve it unchanged, leading to $\mathrm{Im}(\rho_{b,eg})\to\Omega_{pb}/\gamma_2\approx 0.025$. At $t=0.5$ μs we open the coupling field Ω_{cb} to study the transient response of the probe absorption, which gives rise to a new stationary solution $\mathrm{Im}(\rho_{b,eg})\to 0$ at the EIT window $R=R_0$ if $\Delta_{cb}\neq 0$. As for $\Delta_{cb}=0$ we show the dynamics at $R=R_c$. After a 1.0-μs measurement, the control field is switched off again. Figure 4 comparably shows the transient behavior at on resonance or at far-off resonance. The probe absorption $\mathrm{Im}[\rho_{b,eg}(t)]$ tends to be stationary onto new status with different speeds after the first switch on of the coupling $\Omega_{cb}(t)$ at $t=0.5$ μs. It is clear that before the switch on of $\Omega_{cb}(t)$, $\mathrm{Im}[\rho_{b,eg}(t)]$ is the same for all cases due to the decoupled state $|r_b\rangle$, reducing to a two-level scheme. However, once $\Omega_{cb}(t)$ is present the frequency shift of $|r_b\rangle$ will strongly impact the probe absorption. For $\Delta_{cb}=0$ this shift solely caused by the strong probe-target interaction U_{ab}, will lead to a long response time with strong oscillations towards the steady state, typically around $T_{\rm res}=0.90$ μs. Fortunately when U_{ab} is exactly overcome by a finite Δ_{cb} as applied in our scheme, an effective resonant excitation with $\Delta'_{cb}=0$ for the probe atoms could favor a faster response time $T_{\rm res}=0.46$ μs to be stationary. A numerical criterion for stationary state in the calculation is estimated by an average fluctuation of absorption within a time period of 0.1 μs that meets the condition of $|\delta\,\mathrm{Im}(\rho_{b,eg})|<10^{-3}$. Note that the response behavior is totally regardless of the exact Δ_{cb} values because the perfect compensation of Δ_{cb} by a suitable probe-target interaction U_{ab} at a distance R_0, will cause a same resonant two-photon excitation for the probe atoms. So different Δ_{cb} values give rise to exactly the same transient behaviors. Due to the fast response time by an off-resonance spatial EIT, we can safely assume that the atoms are nearly stationary under the cryogenic environment.

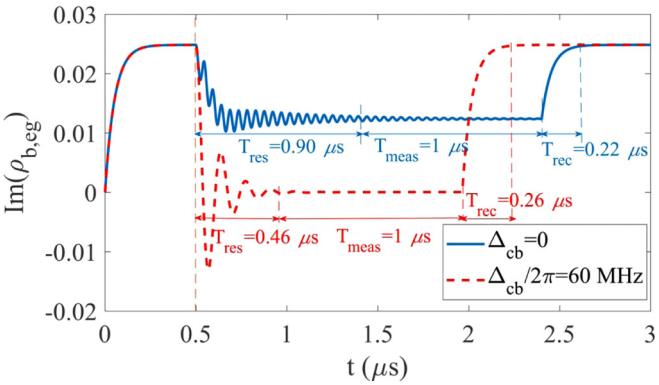

FIG. 4. Transient behavior of the probe absorption $\mathrm{Im}[\rho_{b,eg}(t)]$ as a function of time t undergoing a sudden switch on of the coupling laser at $t=0.5$ μs and a sudden switch off of it after a 1-μs stationary measurement, i.e., $T_{\rm meas}=1.0$ μs. By using $\Delta_{cb}/2\pi=(0,60)$ MHz, the total imaging time which contains response time $T_{\rm res}$, stable measurement $T_{\rm meas}$, and recover time $T_{\rm rec}$, are separately denoted.

After the fast EIT response we set a same time period for carrying out the stable measurement, i.e., 1.0 μs refers to the duration of one-cycle imaging. Then the coupling field $\Omega_{cb}(t)$ is turned off again, raising a similar recovering time back to the original status. Therefore a one-cycle measurement requires totally $T_{\rm res}+T_{\rm meas}+T_{\rm rec}\approx 1.72$ μs (this value becomes 2.12 μs in the IEI case) which could also be regarded as the temporary resolution of our scheme. Repeated measurements via a time-dependent coupling field $\Omega_{cb}(t)$ can be performed on the system where a second 1-μs measurement would have a perfect agreement with the first measurement since they start from the same initial status. Compared to the on-resonant IEI scheme, our method can save the time for one-cycle measurement due to its faster response which enables more repetitive measurements within the duration of Rydberg-state lifetime. To our knowledge, in a real-time imaging process such measurement with fast response can be performed by monitoring the stationary images using a suitable detector, e.g., EMCCD [13]. This detector has shown its preeminent ability in the weak-field measurement because of its ultralow noise, high resolution, high-quantum efficiency, and the robustness to overexposure [41].

IV. MANY-ATOM IMAGING SIMULATION

For the case with more target atoms, we have to perform a many-body quantum simulation following the stationary probability $\rho_{b,eg}(r)$ of each probe atom. Detailed simulation procedures are described in Appendix A. In Fig. 5 we

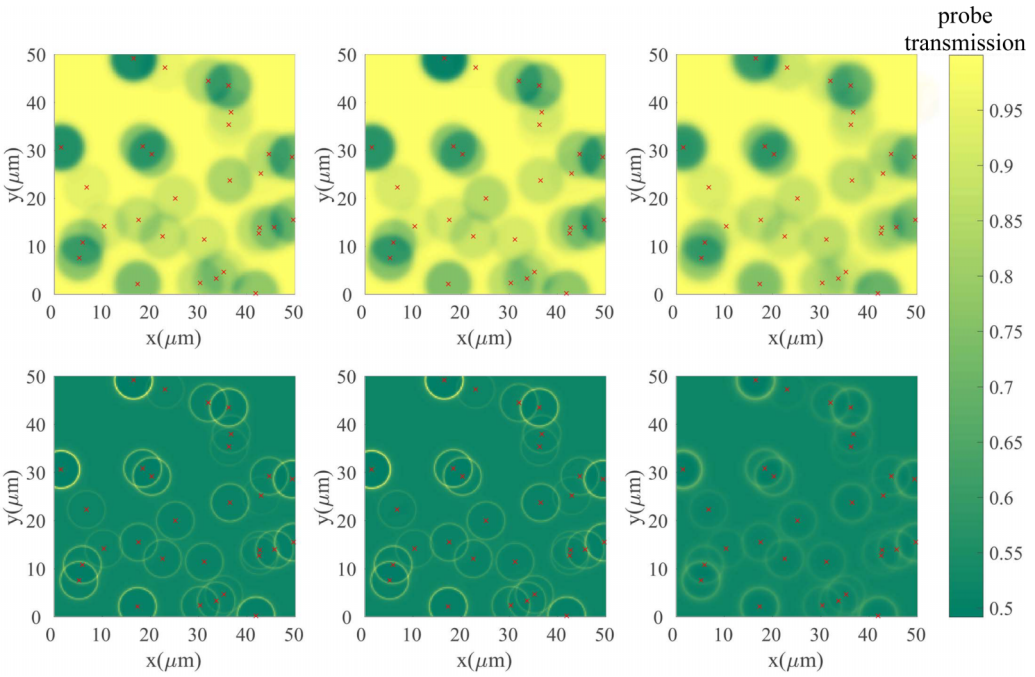

FIG. 5. Simulated many-atom transmission images with 30 randomly distributed target atoms within the area of $(50 \times 50)\ (\mu\text{m})^2$. The red crosses indicate the initial position of target atoms. From top to bottom by increasing the detuning $\Delta_{cb}/2\pi = (0, 60)$ MHz, the transmission images for many atoms become more and more distinguishable with higher spatial resolution, accounting for the dual realization of $R_0 < R_c$ and $\Delta x \ll R_c$ in IETI. From left to right, the thermal motion of target atoms are involved under the temperature T_0 of 0, 10 μK, and 1 mK. The target atoms are preexcited before stationary detection. Sufficient iterations $n_{\max}$ (=1000) are used for preserving a high Rydberg probability of state $|r_a\rangle$ which ensures all targets detectable. Here $(\Omega_{ca}, \Omega_{pa})/2\pi = (1, 10)$ MHz for the Rabi frequencies of target excitation and the precoefficient $C_6^{aa}/2\pi = -1347$ GHz μm^6 used for calculating the vdWs-type interaction between two target atoms, which is $U_{aa} = C_6^{aa}/r_{aa}^6$.

present the transmission images of probe atoms averaging over sufficient one-cycle measurements for resolving the critical position of target atom i. Note that all probe-target U_{ab} and target-target U_{aa} interactions play roles in the calculation. The former produced by the energy shift of state $|r_b\rangle$ can be overcome via an off-resonance detuning Δ_{cb}, giving rise to a precise positioning of target atoms, while the latter decides the Rydberg-state probability of them. The CPT technique with Rabi frequencies $\Omega_{pa} \gg \Omega_{ca}$ ensures a higher excitation probability on average. Once they are sustained on state $|r_a\rangle$ it leads to $\{\rho^i_{a,rr}\} = 1$, in analogy to the single-targe-atom case where the atomic position could be precisely resolved. During one-cycle measurement, after preparation we perform a 1.0-μs stationary measurement. Due to the low temperature as well as the fast response, we safely assume that all target and probe atoms have been stationary. Here we simply use 1.0 μs as the measurement time.

However, due to the finite temperature T_0 which leads to the thermal motion of Rydberg atoms in a real implementation, it may make the transmission ring very blurred. Taking into account the atomic motion, we consider all randomly embedded target atoms move stochastically whose velocities satisfy a two-dimensional Maxwell-Boltzmann distribution

$$f(v_x, v_y) = \frac{m}{2\pi k T_0} \exp\left[-\frac{m(v_x^2 + v_y^2)}{2kT_0}\right] dv_x dv_y \qquad (9)$$

with k the Boltzmann constant, m the atomic mass, and $v_{x(y)}$ the velocity along $\hat{x}(\hat{y})$. Note that we have realized a Doppler-free measurement for probe atoms by letting the probe and coupling fields near perpendicular to the probe atomic motion. To numerically estimate this effect, the position $\vec{r}_i$ of every target atom i is determined by

$$\vec{r}_i \to \vec{r}_i + (v_x\vec{x} + v_y\vec{y})t, \qquad (10)$$

where v_x and v_y are obtained stochastically from the velocity distribution function $f(v_x, v_y)$ characterizing the average thermal speed of target atom i during $T_{\text{meas}} = 1.0\ \mu$s. The variation of $|r_i|$ can modify the probe-target interaction so as to change the radius R_0 of the transmission ring. Our results with 30 target atoms are based on an average over 1000 one-cycle measurements, taking into account all imperfections from atomic movement. Each measurement contains a repetitive Rydberg excitation of target atoms and a stationary measurement for the probe transmission through EIT spectra. Given moving target atoms, the simulated images are obtained by following an integral averaging over the measurement time, as

$$T(x, y) = \frac{1}{T_{\text{meas}}} \int_0^{T_{\text{meas}}} T(x, y, t)dt, \qquad (11)$$

where the stationary target position $\vec{r}_i$ in probe transmission $T(x, y, t)$ is replaced by $\vec{r}_i + \vec{v}t$. It is intuitive that our detection works well in a lower temperature T_0 where the movement of target atoms can be negligible, while a higher T_0 would make the transmission ring drifting and blurred. In addition to the thermal motion of atoms, the heating effect originated from the fluctuation of the laser intensity may also lead to the imperfection of imaging [42]. Nevertheless, in

our scheme a weak probe laser at off resonance gives rise to a poor excitation probability which makes the heating effect less important.

Figure 5 globally illustrates the transmission images of 30 random atoms distributed over a wider regime of $(50 \times 50)\ \mu\text{m}^2$ with (200×200) pixel points. Each pixel has an area of $(0.25\ \mu\text{m})^2$. In the way of traditional IEI (the first row), every target atom can be resolved by detecting the lower-transmission window of the probe EIT, yet suffers from a big reduction of spatial resolution if N_A (the number of target atoms) is large. This is because the image spots decided by the blockade radius R_c significantly overlap in the space as N_A becomes larger, which leads to a poor resolution. For example, in the first row of Fig. 5 each target atom is imaged by a broad disk [see Fig. 3(a1) for single-atom imaging]; the whole image quality becomes very poor due to the overlap among different low-transmission disks. Here different temperatures give rise to less-distinguishable changes because the imaging disk is so broad that a small movement of the central target atom has no visible impact on the imaging pattern. Even at $T_0 = 1\,\text{mK}$ the most probable speed of the target atom is $v_{\text{mps}} \approx 0.4\ \mu\text{m}/\mu\text{s}$ leading to a drifting distance of $0.4\ \mu\text{m}$ which is much smaller than the disk radius R_c.

In our protocol IETI, by tuning Δ_{cb} to be a nonzero value the quality for atomic imaging obtains great improvement as shown in the second row of Fig. 5. Here $\Delta_{cb}/2\pi = 60\,\text{MHz}$ is used. That fact is mainly caused by higher-probe transmission in IETI accompanied by a flexible target-probe spacing R_0 that depends on Δ_{cb}, which leads to a narrow transmission ring for determining the position of all targets. Surely the virtue of IETI also lies in that both the ring radius R_0 and its fluctuating extent Δx can be freely tuned by the detuning Δ_{cb}. Therefore, compared to the IEI scheme in which $\Delta_{cb} = 0$, the presence of a narrow and sharp transmission ring can achieve a higher-resolution imaging of target atomic positions in the IETI scheme. On the other hand, when the temperature T_0 increases to $10\ \mu\text{K}$ in which $v_{\text{mps}} \approx 0.04\ \mu\text{m}/\mu\text{s}$, no visible changes of the image can be found. This is because during measurement, the movement of each target atom i is only $0.04\ \mu\text{m}$, which is smaller than the ring thickness Δx by one order of magnitude. Only if T_0 is increased to be 1 mK, which is higher than a typical experimental temperature, a moving target atom will fluctuate the probe-target interaction U_{ab}, making the image slightly faint because $v_{\text{mps}} T_{\text{meas}} \approx \Delta x$. A rough estimation for a maximal temperature that our scheme works is about 1 mK because if the drifting distance of the transmission ring is larger than the ring width, i.e., $v_{\text{mps}} T_{\text{meas}} > \Delta x$, it is impossible to determine its central position with high precision. Also, we see the image contrast on the ring suffers from a clear reduction. The reason comes from an average over 1000 one-cycle measurements in which the slim ring is sensitive to the position of target atoms, i.e., the slim ring would be drifted in every measurement. As a consequence, the final detected image becomes lower contrast and blurred as the temperature increases.

V. FEASIBILITY DISCUSSION AND CONCLUSION

Now we discuss the scheme feasibility by assessing the signal-to-noise ratio (SNR) during the IETI measurement. The

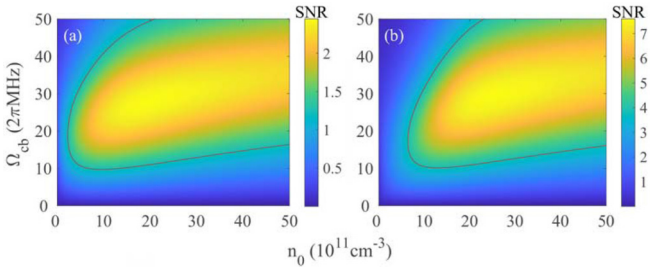

FIG. 6. Estimated SNR with the parameters (n_0, Ω_{cb}) when the exposure time is (a) $t_{\text{exp}} = 1\ \mu\text{s}$ and (b) $t_{\text{exp}} = 10\ \mu\text{s}$. The solid line in each plot depicts the contour of $R_{S/N} = 1$. Other systematic parameters are $a = 0.16\ (\mu\text{m})^2$, $\sigma_0 = 0.145\ (\mu\text{m})^2$, $\Gamma_{eg}/2\pi = 6.1\,\text{MHz}$, $A = 10\ (\mu\text{m})^2$, $L_z = 10\ \mu\text{m}$, and $T_0 = 0\,\text{K}$.

noise in the measurement typically comes from the shot noise of photons and of atoms, respectively. They are described by a variance of the transmission signal ΔT [10]:

$$\text{var}(\Delta T) \approx \frac{2 + \langle T\rangle + \langle T\rangle^2}{\langle N_r\rangle} + \frac{\sigma_0^2 n L_z}{a}\text{Im}(\chi)^2\langle T\rangle^2, \quad (12)$$

where the first term is attributed to the Poisson distributed photon shot noise and the second term is from probe atomic density fluctuations. ΔT is the relative transmission rate with respect to that from a reference image generated in the case of no target atoms. σ_0 is the probe absorption cross section. To ensure that the density of the Rydberg probe atoms is kept low and the EIT condition $\Omega_{pb} \ll \Omega_{cb}$ is satisfied, we assume $\Omega_{pb}^2 = 0.1\Omega_{cb}^2 n_0 L_z A$. In the limit of the strongest transmission $\langle T\rangle \approx 1.0$ we assume the mean photon number at each pixel is $\langle N_r\rangle \approx 0.1 a t_{\text{exp}} \Omega_{cb}^2/\sigma_0 n_0 L_z \Gamma_{eg} A$ with $A = 2\pi R_0 \Delta x$ for the ring area, n_0 the peak density, a the area of each pixel, and t_{exp} the exposure time determined by the stable measurement time T_{meas}. Hence, Eq. (12) can be explicitly rewritten as

$$\text{var}(\Delta T) = \frac{\sigma_0 \Gamma_{eg} n_0 L_z A}{10 a \Omega_{cb}^2 t_{\text{exp}}} \times \left(4 + \frac{\Omega_{cb}^2 t_{\text{exp}} \sigma_0 \text{Im}(\chi)^2}{A\Gamma_{eg}} e^{-2\sigma_0 n_0 L_z \text{Im}(\chi)}\right) \quad (13)$$

with $\text{Im}(\chi) = (1 + 0.2\Omega_{cb}^2/\Gamma_{eg} A n L_z)^{-1}$ characterizing the probe absorption. One can define $R_{S/N} = \Delta T/\sqrt{\text{var}(\Delta T)}$, which has to be larger than 1 for detecting the target atoms in the imaging.

In Figs. 6(a) and 6(b) the numerical estimation for SNR distribution is represented when both the peak atomic density n_0 and the coupling strength Ω_{cb} are adjusted for different exposure times. Note that the SNR is relatively smaller as compared to the earlier IEI schemes [12], since we require smaller pixels to image the slim transmission ring, which may add a larger shot noise due to $\text{var}(\Delta T) \propto a^{-1}$. Here we choose each pixel containing the width of ring and hence the pixel area is $a = (\Delta x)^2 \approx (0.4\ \mu\text{m})^2$, following the parameters in Fig. 3(a2). By comparing the simulation results of Figs. 6(a) and 6(b) where the atomic movement is ignored, we observe that for $t_{\text{exp}} = 1\ \mu\text{s}$, the optimal SNR is sustained above 1.0 at appropriate n_0 or Ω_{cb} values. And a longer-time measurement $t_{\text{exp}} = 10\ \mu\text{s}$ will raise a larger SNR because of the continuous excitation of probe atoms. Extra imperfections such as atomic

thermal motion brought on by a longer exposure time will be left for consideration in the future. A rough estimation of the mean photon number based on each pixel arises: $\langle N_r \rangle \approx 0.5$ for $n_0 = 5 \times 10^{11}$ cm^{-3} and $t_{\rm exp} = 1$ μs. Another obstacle arises with the increase of probe atomic density n_0, which is the avalanche effect. This effect makes it possible to excite more nearby probe atoms to the Rydberg state, destroying an accurate positioning of every target atom. Luckily it is difficult to observe the avalanche excitation since the maximal probe excitation rate $\rho_{b,rr}^{\max} \propto (\Omega_{pb}/\Omega_{cb})^2 = 10^{-4}$ is very low even at resonance, which cannot reach the critical point as reported in Refs. [43,44].

In conclusion, we propose an improved IETI technique for the nondestructive determination of atom positions with both high spatial resolution and fast response time. This increased resolution compared to the previous IEI method is mainly attributed to the use of an off-resonant spatial EIT excitation with respect to the background probe atoms. Once the probe detuning of Rydberg levels suitably overcomes the strong probe-target interaction, it induces an extremely narrow absorption dip at a critical probe-target distance. One can precisely resolve the location of the target atoms by using this narrow window, attaining a spatial fluctuation of about 0.4 μm constrained by the optical diffraction limit. Furthermore, a higher resolution is expected in the IETI approach via the adjustment of detuning solely. The IETI approach not only preserves the merits of the traditional IEI method, which is a nondestructive and state-sensitive technique, but also promises a challenge of superresolution Rydberg imaging ascribed to the new control knob from an off-resonance EIT excitation to the background probe atoms. The response time for single measurement also obtains a great improvement in IETI which is suitable for a present practical performance. All the parameters we use to optimize the simulated images closely meet with the current experimental conditions, deserving of experimental exploration with cold Rydberg atoms in a practical ensemble.

To exceed the diffraction limit determined by the imaging laser field, existing techniques often utilize point-to-point image reconstruction with multiple measurements per point by scanning or labeling [45,46]. For example, stochastic optical reconstruction microscopy (STORM), is eligible to be applied here to overcome this limit. The principle of STORM is to utilize a few photons for each shot of imaging but consecutively sufficient photons to enable precise localization [46]. Equations (3) and (5) imply that the EIT spatial imaging is independent of the intensity of the probe laser and therefore the IETI technique works with a low-light-level probe imaging beam. With the photon number of the probe laser reduced to a few photons, we expect that the best spatial resolution reaches tens of nanometers. Moreover, machine learning (ML) can accomplish the task of classification and identification of complex image patterns, so it can robustly improve the process of image recognition by providing training data based on resembling experimental data, not on idealized theoretical predictions [47]. Optical reconstruction techniques based on a ML algorithm may initiate another fast and accurate characterization of object structures and provide a promising approach for our scheme to reach superresolution many-atom imaging in the future [48].

ACKNOWLEDGMENTS

This work is supported by the National Key Research and Development Program of China under Grants No. 2016YFA0302001 and No. 2019ZT08X324; by the National Natural Science Foundation of China under Grants No. 12174106, No. 11474094, No. 11104076, and No. 11654005; by Guangdong Provincial Key Laboratory under Grant No. 2019B121203002; by the Science and Technology Commission of Shanghai Municipality under Grant No. 18ZR1412800; by the Shanghai Municipal Science and Technology Major Project under Grant No. 2019SHZDZX01; and also additional support from the Shanghai talent program.

APPENDIX A: QUANTUM SIMULATION

Rydberg preparation of multitarget atoms. The transmission imaging signal can be numerically simulated via a semiclassic Monte Carlo approach [49]. The target energy levels as presented in Fig. 1(b), adopt a two-photon excitation with $|g_a\rangle = |5S_{1/2}\rangle$, $|e_a\rangle = |5P_{3/2}\rangle$, and $|r_a\rangle = |85S_{1/2}\rangle$. The optical couplings among them are $\Omega_{ca}/2\pi = 1$ MHz and $\Omega_{pa}/2\pi = 10$ MHz. Given the initial status with all target atoms in the ground states $|g_a\rangle$ we assume an initial one-dimensional array for denoting their status

$$\{\{\rho_{a,rr}^i\}\}_{n=0} = \{0, 0, 0, \ldots, 0, 0, \ldots\}, \tag{A1}$$

where the superscript i represents the ith embedded target atom, and denotation $\{\rho_{a,rr}^i\} = 1$ or 0 means that the target atom is excited to $|r_a\rangle$ or not. The stationary Rydberg probability $\rho_{a,rr}^i$ of the ith atom is given by [50]

$$\rho_{a,rr}^i = \frac{|\Omega_{pa}|^2(|\Omega_{pa}|^2 + |\Omega_{ca}|^2)}{(|\Omega_{pa}|^2 + |\Omega_{ca}|^2)^2 + (\gamma_{ea}^2 + 2|\Omega_{pa}|^2)\delta_i^{(n)}}, \tag{A2}$$

where $\gamma_{ea}/2\pi = 6.1$ MHz. $\rho_{a,rr}^i$ varies with the two-photon detuning $\delta_i^{(n)}$ and for $\delta_i^{(n)} = 0$ it attains a maximal value.

Initially $n = 0$ we assume a resonant two-photon detuning $\delta_i^{(0)} = \Delta_{pa} + \Delta_{ca} = 0$, giving rise to a maximal probability $\rho_{a,rr}^i$. No target-target interaction presents initially. Next one generates a random number s_i between (0,1) for each target atom i. If $s_i \leqslant \rho_{a,rr}^i$ we set $\{\rho_{a,rr}^i\} = 1$ (excited), otherwise, $\{\rho_{a,rr}^i\} = 0$ (not excited). That will give rise to a new array, for example $\{\{\rho_{a,rr}^i\}\}_n = \{0, 1, 0, 0, \ldots, 0, 1, 0, 1, 0, \ldots\}$ with $n = 1, 2, \ldots, n_{\max}$ representing the iterations. $\{\{\rho_{a,rr}^i\}\}_n$ denotes the updated status of all target atoms.

For the ith target atom, any other target atom j in the Rydberg state $|r_a\rangle$, i.e., $\{\rho_{a,rr}^j\} = 1$, will induce a target-target level shift, translating into the ith-atom two-photon detuning δ_i, given by

$$\delta_i^{(n+1)} = \delta_0 + \sum_{j \neq i}^{N_A} \left\{\rho_{a,rr}^i\right\}_n \frac{C_6^{aa}}{|r_j - r_i|^6}. \tag{A3}$$

For the initial step, $n = 0$ and $\delta_i^{(0)} = \delta_0$. N_A is the number of target atoms and $\frac{C_6^{aa}}{|r_j - r_i|^6}$ stands for the intraspecies vdWs interactions between i-j target atoms that possess Rydberg S state via a two-photon excitation with $C_6^{aa}/2\pi = -1347.2$ GHz [32].

Finally a large number of target atoms would be prepared on $|r_a\rangle$, giving rise to the final status of all target atoms, e.g.,

$$\left\{\left\{\rho^i_{a,rr}\right\}\right\}_{n_{\max}} = \{1, 1, 1, \ldots, 0, 1, \ldots\} \tag{A4}$$

under sufficient iterations. The maximum $n_{\max}$ depends on the excitation parameters used for target atoms. In particular, when two or more target atoms are initially closely placed within the target blockade radius it is difficult to simultaneously excite them owing to the blockade effect. However the probability for that is tiny. Therefore, by using sufficient iterations for Rydberg preparation the average excitation probability of the ith atom, finally expressed as

$$\bar{\rho}_i = \frac{1}{n_{\max}} \sum_{n=1}^{n_{\max}} \left\{\rho^i_{a,rr}\right\}_n, \tag{A5}$$

is very close to 1.0. Note that if any target atom remains unexcited after n iterations it cannot be detected in the imaging process due to the absence of the probe-target interaction. To avoid this, we repeatedly pump the target atoms from the ground state before detection. We note that during the detection process these preexcited target atoms can be sustained on the Rydberg state and thus a nondestructive measurement using off-resonant Rydberg EIT, can be performed.

Detection for transmitted probe light. Given the preexcitation status of target atoms, we can calculate the stationary probe absorption at off-resonance by following Eq. (3), where the effective two-photon detuning $\delta(r)$ reflecting the probe-target interaction is replaced by

$$\delta(r) = \Delta_{cb} - \sum_{i(r_i \neq r)}^{N_A} \left\{\rho^i_{a,rr}\right\} \frac{C_6^{ab}}{|r - r_i|^6}. \tag{A6}$$

For any atom i only the surrounding probe atoms with a suitable relative distance $|r - r_i|$ that leads to $\delta(r) \approx 0$, can reveal a sharp absorption dip in the off-resonant EIT spectra. Other unsuited probe atoms cannot be detected. Based on the modified Eq. (3) as well as Eq. (4), it arrives at the first-order susceptibility $\chi(r)$ whose imaginary part stands for the probe absorption rate. The probe transmission is proportional to $|\exp[i\chi(r)]|$ following Eq. (7). By plotting the probe-atom transmission in the (x, y) space we can capture the information of preexcited target atoms. Due to the high-quality images of transmission spectra which contain position-sensitive and great resolution advantages, target atoms can be clearly resolved for single-time measurement. Stable exposure time required by a typical detector is about a few microseconds so here, i.e., the measurement time $T_{\text{meas}} = 1.0\ \mu$s is assumed [11].

Therefore in our simulation, all target-target interactions coming from repeated excitations of target atoms, do perform only in the preexcitation process. Once two random target atoms are closely placed within the blockade range for target atoms, this imperfect Rydberg preparation would make the measurement fail. To make all target atoms detectable, we have to perform repeated excitation runs before measurement and finally obtain an average excitation probability $\bar{\rho}_i$ which is very close to 1.0. In addition, all probe-target interactions are considered as long as the target atoms are excited. The enhanced transmission signal closing to 100% emerges at the absorption dip due to an off-resonant EIT effect of probe atoms. Differing from the previous IEI scheme using resonant EIT, the off-resonant EIT condition favors a narrower transmission window which promises a higher spatial-resolution image.

Note that in Sec. IV the probe-probe interaction has been ignored accounting for the poor exciting probability of probe atoms at the off-resonant EIT condition. Even in the vicinity of the transmission ring in which the two-photon detuning is overcome by the probe-target interaction, the weak-driving condition as well as the sufficient measurements can ensure the impact of probe excitation is negligible. A detailed discussion for the probe-probe interaction is presented in Appendix B. In the calculation we adopt sufficient iternations $n_{\max}$ ensuring the Rydberg excitation of target atoms. So the final results involving the target-target as well as the probe-target vdWs interactions, can return accurate positions of randomly distributed target atoms in a two-dimensional space, as displayed in Figs. 3 and 5.

APPENDIX B: INFLUENCE OF THE PROBE-PROBE INTERACTIONS

Theoretical derivation of the probe-probe interactions. For probe atoms they have an off-resonant excitation suffering from a poor excitation probability. However, once the atom is placed near the transmission ring with a certain distance R_0 to the target atom, due to strong target-probe vdWs interaction that may overcome the two-photon detuning Δ_{cb}, the probe excitation becomes resonant. In this Appendix we focus on the impact of the probe-probe interactions.

For probe atoms, we consider the following soft-core potential [51,52]:

$$U_{bb} = \begin{cases} -\frac{3^6 C_6^{bb}}{R_c'^6}, & \text{if } 0 < r' \leqslant \frac{1}{3}R_c' \\ -\frac{C_6^{bb}}{r'^6}, & \text{if } r' > \frac{1}{3}R_c' \end{cases} \tag{B1}$$

with $R_c' = 5.7\ \mu$m the blockade radius of probe atoms and r' the probe-probe distance. The presence of the probe-probe interaction would modify the effective two-photon detuning $\delta(r)$ in Eq. (4) with respect to the probe atom, which is

$$\delta(r) = \Delta_{cb} - \frac{C_6^{ab}}{R^6} - \int_0^\infty U_{bb} n \rho_{b,rr}(r') d^3\boldsymbol{r}'. \tag{B2}$$

Here the probe atomic density n is a function of position due to the Gaussian profile of atomic cloud, with its peak value $n_0 = 5 \times 10^{11}\ \text{cm}^{-3}$ as described in Eq. (5), and $\boldsymbol{r}'$ denotes the relative distance between two probe atoms. The probe-probe interaction coefficient $C_6^{bb}/2\pi = -662.4\ \text{GHz}\,\mu\text{m}^6$. The average Rydberg excitation probability $\rho_{b,rr}$ of probe atom can be analytically solved by [50]

$$\rho_{b,rr}(r') = \frac{|\Omega_{pb}|^2(|\Omega_{pb}|^2 + |\Omega_{cb}|^2)}{(|\Omega_{pb}|^2 + |\Omega_{cb}|^2)^2 + \left(\gamma_2^2 + 2|\Omega_{pb}|^2\right)\delta(r')} \tag{B3}$$

due to its two-photon excitation feature.

We carry out a rough estimation for the maximal probe-probe interaction U_{bb} [the third term in Eq. (B2)]. At resonance $\delta(r) \approx 0$ leading to a maximal Rydberg fraction $\rho_{b,rr}^{\max} \propto (\Omega_{pb}/\Omega_{cb})^2 = 10^{-4}$ by considering $\Omega_{pb}/2\pi = 0.15\,\text{MHz}$ and $\Omega_{cb}/2\pi = 15\,\text{MHz}$ in the weak probe regime.

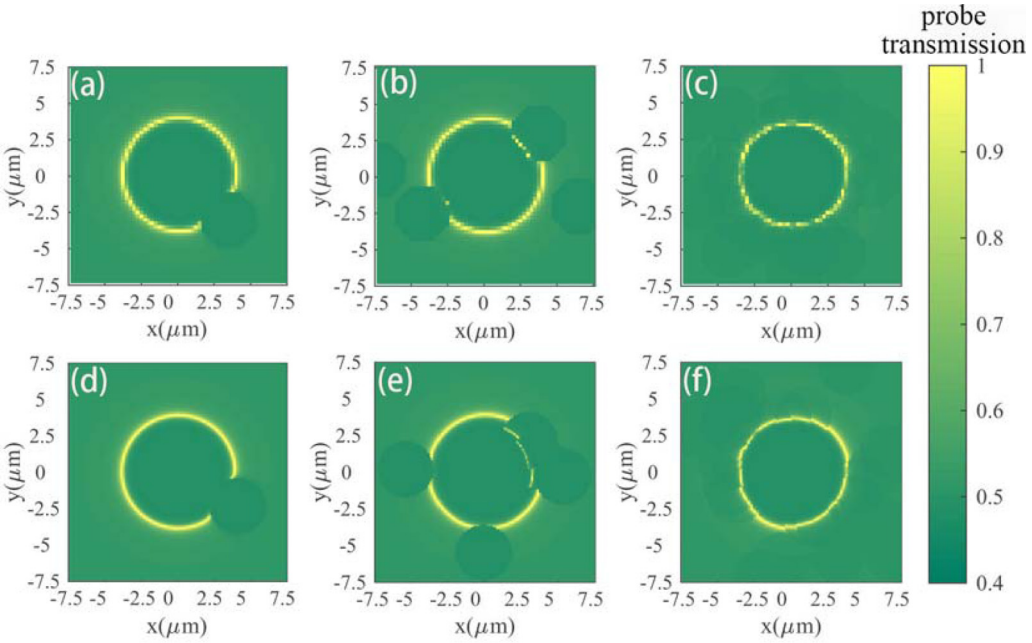

FIG. 7. Numerical representation of the single-target atom image with probe-probe interactions, covering the range of $(15 \times 15)\ \mu\text{m}^2$ for (a)–(c) 60×60 pixels and (d)–(f) 150×150 pixels. Areas of each pixel are $(0.25\ \mu\text{m})^2$ and $(0.1\ \mu\text{m})^2$, respectively. From left to right, different iterations (repeated measurements) are used which are 10, 100, and 1000. Other parameters are adopted from Fig. 3(a2).

By replacing the above parameters, the maximal U_{bb} enabled by the nearest-neighbor probe atoms at resonance, is

$$U_{bb}^{\max} = n_0 \rho_{b,rr}^{\max} \int_0^{\Delta x} U_{bb}(r') d^3\boldsymbol{r}' \approx -1.26\ \text{MHz}. \tag{B4}$$

Actually at the off-resonant case the influence of U_{bb} can be safely ignored due to $|U_{bb}| \ll \Delta_{cb}$. However, as closing to the transmission ring the cancellation of Δ_{cb} by a suitable probe-target interaction U_{ab} may make the U_{bb} important [see Eq. (B2)]. We will study the impact of probe-probe interactions using two numerical methods.

Stationary images with probe-probe interactions. One way to resolve the single-target-atom images with probe-probe interactions may be to use a similar approach as described in Appendix A. Given the initial status of ground probe atoms on $|g_b\rangle$, we assume

$$\left\{\left\{\rho_{b,rr}^i\right\}\right\}_{n=0} = \{0, 0, 0, \ldots, 0, 0, \ldots\}, \tag{B5}$$

where the superscript i represents the probe atoms at the ith pixel, and here 60×60 and 150×150 pixels have been respectively simulated in a $(15 \times 15)\ \mu\text{m}^2$-2D plane. $\{\rho_{b,rr}^i\} = 1$ or 0 means that the probe atom is excited to the Rydberg state $|r_b\rangle$ or not. The stationary Rydberg probability $\rho_{b,rr}^i$ of the ith atom at initial step $n = 0$ is expressed as

$$\rho_{b,rr}^i \approx \frac{|\Omega_{pb}|^2(|\Omega_{pb}|^2 + |\Omega_{cb}|^2)}{(|\Omega_{pb}|^2 + |\Omega_{cb}|^2)^2 + \left(\gamma_2^2 + 2|\Omega_{pb}|^2\right)\delta_0^2}, \tag{B6}$$

due to a two-photon excitation, where a resonant two-photon detuning $\delta_0 = \Delta_{cb} + U_{ab}$ is considered. No probe-probe interaction presents at the initial time.

The probability denoting the probe-atom excitation within the ith pixel, is computed as

$$P_{rr}^i = nL_z dx\, dy\, \rho_{b,rr}^i, \tag{B7}$$

where $N_b = nL_z dx\, dy \ll 1$ is the average number of probe atoms in each pixel. L_z is the z-axis thickness of atomic medium, and dx and dy are respectively the x-axis and y-axis length of the pixel, with n the number density of probe atoms. No more than one probe atom can be excited to the Rydberg state $|r_b\rangle$ within the same pixel due to the blockade effect.

Next, one generates a random number s_i between (0,1) for each pixel i. If $s_i \leqslant P_{rr}^i$ we set $\{\rho_{b,rr}^i\} = 1$ (excited), otherwise, $\{\rho_{b,rr}^i\} = 0$ (not excited). That will give rise to a new array of $\{\{\rho_{b,rr}^i\}\}_n$ with $n = 1, 2, \ldots, n_{\max}$ representing the iterations. $\{\{\rho_{b,rr}^i\}\}_n$ denotes the updated status of all probe atoms. For the probe atom in the ith pixel, if any other probe atom in the jth pixel is in the Rydberg state $|r_b\rangle$, i.e., $\{\rho_{b,rr}^j\} = 1$, it will induce a probe-probe level shift, translating into the ith-atom two-photon detuning δ_i given by

$$\delta_i^{(n+1)} = \delta_0 + \sum_{j \neq i}^{N_B} \left\{\rho_{b,rr}^i\right\}_n U_{i,j} \tag{B8}$$

with N_B the number of pixels and $U_{i,j}$ the intraspecies vdWs interaction between i-j probe atoms, using the way of the soft-core model as in Eq. (B1). For the initial step $n = 0$ and $\delta_i^{(0)} = \delta_0$. As a result, by using sufficient iteration the final average probe-probe interaction of each pixel is actually given by

$$\bar{U}_{bb}^i = \frac{1}{n_{\max}} \sum_{n=1}^{n_{\max}} \sum_{j \neq i}^{N_B} \left\{\rho_{b,rr}^i\right\}_n U_{i,j}. \tag{B9}$$

Then the susceptibility and the transmission of each pixel are given by Eqs. (5) and (7).

Figure 7 represents the single-atom imaging with the influence of the probe-probe interactions. It is clearly shown that

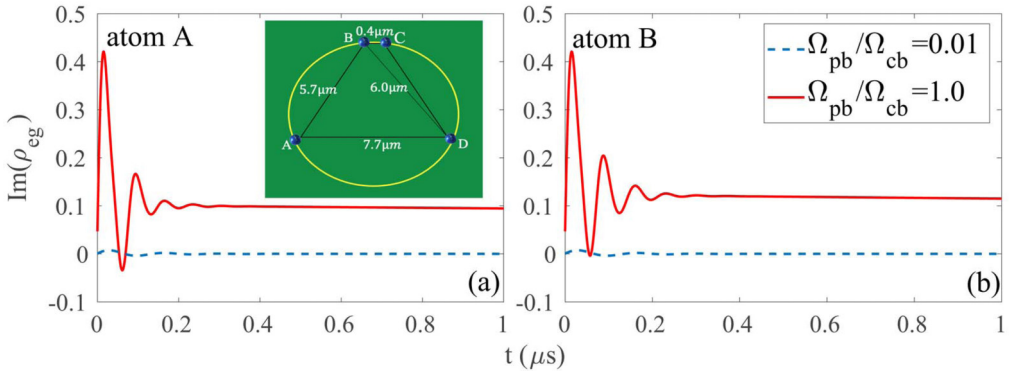

FIG. 8. (a),(b) The absorption Im$[\rho_{eg}(t)]$ for two resonantly excited probe atoms A and B. Results from different Rabi frequencies $\Omega_{pb}/\Omega_{cb} = (0.01, 1.0)$ are shown. Here $\Omega_{cb}/2\pi = 15$ MHz.

when the iteration is insufficient the image is incomplete [see Figs. 7(a) and 7(b) and 7(d) and 7(e)] due to the probe-probe interaction. This is because the accidental excitation of the probe atom in single measurement will lead to the breakdown of the transmission conditions at R_0, making the transmission ring incomplete. However, after performing sufficient measurements an average result can also form a complete transmission ring at the expense of a little brightness [see Fig. 7(c)]. In addition we observe that a low pixel (precision) could cause the images to be blurred. However, once a sufficient iteration is applied, e.g., $n_{\max} = 1000$, accompanied by a precise measurement (high pixel) an expected transmission ring can be reobserved by averaging the influence of the probe-probe interactions. By comparing Figs. 7(c) and 3(a2), it is confirmed that we can approximately ignore U_{bb} in the calculation.

Absorption of a few probe atoms with probe-probe interactions. To quantitatively discuss the influence of probe-probe interaction we introduce a simple model containing four control atoms at the transmission ring and one target atom in the center [see inset of Fig. 8(a)]. Note that an excited target atom would only lead to a resonant two-photon excitation for probe atoms on the ring. So we can exactly solve the probe-atom evolution by using a few-body master equation excluding the target atom,

$$\dot{\rho} = -i[\mathcal{H}, \rho] + \mathcal{L}[\rho], \tag{B10}$$

where the density matrix ρ becomes a $3^4 \times 3^4$ matrix. As a result the Hamiltonian composing all atom-field and atom-atom interactions, can be written as

$$\mathcal{H} = -\sum_{i=1}^{4}\left(\frac{\Omega_{pb}}{2}\sigma_{eg}^{i} + \frac{\Omega_{cb}}{2}\sigma_{re}^{i} + \text{H.c.}\right) + \sum_{i<j}\sigma_{rr}^{i}\frac{C_6^{bb}}{r_{ij}^6}\sigma_{rr}^{j} \tag{B11}$$

with $\sigma_{\mu\nu}^{i} \equiv |\mu_i\rangle\langle\nu_i|$ and r_{ij} the probe-probe distance. The Liouville operator $\mathcal{L} = \sum_{i=1}^{4}(\mathcal{L}_e^i + \mathcal{L}_r^i)$ is expressed as a sum of independent single-atom decay of state $|e_b\rangle$ and dephasing of state $|r_b\rangle$, with $\mathcal{L}_e^i = \frac{\gamma_2}{2}\sum_{i=1}^{4}(2\sigma_{ge}^i\rho\sigma_{eg}^i - \{\sigma_{ee}^i, \rho\})$ and $\mathcal{L}_r^i = \gamma_3\sum_{i=1}^{4}[(\sigma_{rr}^i - \sigma_{gg}^i)\rho(\sigma_{rr}^i - \sigma_{gg}^i) - \rho]$ [34].

Given the peak atomic density $n_0 = 5 \times 10^{11}$ cm^{-3} we assume two atoms B and C are closely placed with a distance of $1/(n_0 L_z)^{1/2} \approx 0.4$ μm, in which the probe-probe interaction is dominant. Other atoms are far separated. By solving the master equation (B10) with full probe-probe interactions we could numerically solve the probe absorption Im$[\rho_{eg}(t)]$ during the measurement time for atoms A and B. Note that due to the symmetrical structure the behavior of atom D (C) is equal to that of atom A (B). Comparing Figs. 8(a) and 8(b), it is clear that the absorptions of atoms A and B have perfect agreement if $\Omega_{pb}/\Omega_{cb} = 0.01$ (blue dashed line) as used in our work. This is because the weak excitation of the probe atoms, even at the transmission ring where two-photon resonance is met, will make the impact of the probe-probe interaction negligible. Only if Ω_{pb}/Ω_{cb} is raised to 1.0 (red solid line), which leads to a significant excitation of the probe atoms, the steady absorption of atom B will be slightly higher than that of atom A which is caused by different probe-probe strengths felt by atoms A and B. This simulation again confirms that the probe-probe interaction can be safely ignored in our approach.

[1] A. Schwarzkopf, R. E. Sapiro, and G. Raithel, Imaging Spatial Correlations of Rydberg Excitations in Cold Atom Clouds, Phys. Rev. Lett. **107**, 103001 (2011).

[2] P. McQuillen, X. Zhang, T. Strickler, F. B. Dunning, and T. C. Killian, Imaging the evolution of an ultracold strontium Rydberg gas, Phys. Rev. A **87**, 013407 (2013).

[3] P. Schauss, M. Cheneau, M. Endres, T. Fukuhara, S. Hild, A. Omran, T. Pohl, C. Gross, S. Kuhr, and I. Bloch, Observation of spatially ordered structures in a two-dimensional Rydberg gas, Nature (London) **491**, 87 (2012).

[4] H. Labuhn, D. Barredo, S. Ravets, S. De Leseleuc, T. Macri, T. Lahaye, and A. Browaeys, Tunable two-dimensional arrays of single Rydberg atoms for realizing quantum Ising models, Nature (London) **534**, 667 (2016).

[5] M. Saffman, T. G. Walker, and K. Mølmer, Quantum information with Rydberg atoms, Rev. Mod. Phys. **82**, 2313 (2010).

[6] V. Giovannetti, S. Lloyd, and L. Maccone, Advances in quantum metrology, Nat. Photonics **5**, 222 (2011).

[7] S. Garcia, M. Stammeier, J. Deiglmayr, F. Merkt, and A. Wallraff, Single-Shot Nondestructive Detection of Rydberg-Atom Ensembles by Transmission Measurement of a Microwave Cavity, Phys. Rev. Lett. **123**, 193201 (2019).

[8] C. Veit, N. Zuber, O. A. Herrera-Sancho, V. S. V. Anasuri, T. Schmid, F. Meinert, R. Löw, and T. Pfau, Pulsed Ion Microscope to Probe Quantum Gases, Phys. Rev. X **11**, 011036 (2021).

[9] B. Olmos, W. Li, S. Hofferberth, and I. Lesanovsky, Amplifying single impurities immersed in a gas of ultracold atoms, Phys. Rev. A **84**, 041607(R) (2011).

[10] G. Günter, M. Robert-de Saint-Vincent, H. Schempp, C. S. Hofmann, S. Whitlock, and M. Weidemüller, Interaction Enhanced Imaging of Individual Rydberg Atoms in Dense Gases, Phys. Rev. Lett. **108**, 013002 (2012).

[11] G. Günter, H. Schempp, M. Robert-De-Saint-Vincent, V. Gavryusev, S. Helmrich, C. S. Hofmann, S. Whitlock, and M. Weidemueller, Observing the dynamics of dipole-mediated energy transport by interaction-enhanced imaging, Science **342**, 954 (2013).

[12] V. Gavryusev, M. Ferreira-Cao, A. Kekic, G. Zürn, and A. Signoles, Interaction-enhanced imaging of Rydberg *P* states, Eur. Phys. J.: Spec. Top. **225**, 2863 (2016).

[13] C. Gross, T. Vogt, and W. Li, Ion Imaging via Long-Range Interaction with Rydberg Atoms, Phys. Rev. Lett. **124**, 053401 (2020).

[14] M. Huo, Spatial imaging of the movement of bound atoms to reveal the Rydberg molecular bond via electromagnetically induced transparency, Europhys. Lett. **118**, 43001 (2017).

[15] W. Xu, A. V. Venkatramani, S. H. Cantú, T. Šumarac, V. Klüsener, M. D. Lukin, and V. Vuletić, Fast Preparation and Detection of a Rydberg Qubit Using Atomic Ensembles, Phys. Rev. Lett. **127**, 050501 (2021).

[16] H. Gorniaczyk, C. Tresp, P. Bienias, A. Paris-Mandoki, W. Li, I. Mirgorodskiy, H. P. Büchler, I. Lesanovsky, and S. Hofferberth, Enhancement of Rydberg-mediated single-photon nonlinearities by electrically tuned Förster resonances, Nat. Commun. **7**, 12480 (2016).

[17] F. Engel, T. Dieterle, T. Schmid, C. Tomschitz, C. Veit, N. Zuber, R. Löw, T. Pfau, and F. Meinert, Observation of Rydberg Blockade Induced by a Single Ion, Phys. Rev. Lett. **121**, 193401 (2018).

[18] Z. Zhang, Y. Peng, C. Li, Z. Jia, and Q. Zeng, Proposal for measurement of the van der Waals interaction in a cold Rydberg ensemble via electromagnetically induced transparency, J. Opt. Soc. Am. B **36**, 2216 (2019).

[19] I. Novikova, R. L. Walsworth, and Y. Xiao, Electromagnetically induced transparency-based slow and stored light in warm atoms, Laser Photonics Rev. **6**, 333 (2012).

[20] Y.-C. Yu, M.-X. Dong, Y.-H. Ye, G.-C. Guo, D.-S. Ding, and B.-S. Shi, Experimental demonstration of switching entangled photons based on the Rydberg blockade effect, Sci. China Phys. Mech. Astron. **63**, 1 (2020).

[21] A. K. Mohapatra, T. R. Jackson, and C. S. Adams, Coherent Optical Detection of Highly Excited Rydberg States Using Electromagnetically Induced Transparency, Phys. Rev. Lett. **98**, 113003 (2007).

[22] S. Baur, D. Tiarks, G. Rempe, and S. Dürr, Single-Photon Switch Based on Rydberg Blockade, Phys. Rev. Lett. **112**, 073901 (2014).

[23] J. D. Pritchard, D. Maxwell, A. Gauguet, K. J. Weatherill, M. P. A. Jones, and C. S. Adams, Cooperative Atom-Light Interaction in a Blockaded Rydberg Ensemble, Phys. Rev. Lett. **105**, 193603 (2010).

[24] D. Petrosyan, J. Otterbach, and M. Fleischhauer, Electromagnetically Induced Transparency with Rydberg Atoms, Phys. Rev. Lett. **107**, 213601 (2011).

[25] D. W. Schönleber, A. Eisfeld, M. Genkin, S. Whitlock, and S. Wüster, Quantum Simulation of Energy Transport with Embedded Rydberg Aggregates, Phys. Rev. Lett. **114**, 123005 (2015).

[26] V. Gavryusev, A. Signoles, M. Ferreira-Cao, G. Zürn, C. S. Hofmann, G. Günter, H. Schempp, M. Robert-De-Saint-Vincent, S. Whitlock, M. Weidemüller *et al.*, Density matrix reconstruction of three-level atoms via Rydberg electromagnetically induced transparency, J. Phys. B: At., Mol. Opt. Phys. **49**, 164002 (2016).

[27] A. Urvoy, F. Ripka, I. Lesanovsky, D. Booth, J. P. Shaffer, T. Pfau, and R. Löw, Strongly Correlated Growth of Rydberg Aggregates in a Vapor Cell, Phys. Rev. Lett. **114**, 203002 (2015).

[28] U. Raitzsch, R. Heidemann, H. Weimer, B. Butscher, P. Kollmann, R. Löw, H. P. Büchler, and T. Pfau, Investigation of dephasing rates in an interacting Rydberg gas, New J. Phys. **11**, 055014 (2009).

[29] R. W. Boyd, *Nonlinear Optics* (Academic, New York, 2020).

[30] M. Xiao, T.-Q. Li, S.-Z. Jin, and J. Gea-Banacloche, Measurement of Dispersive Properties of Electromagnetically Induced Transparency in Rubidium Atoms, Phys. Rev. Lett. **74**, 666 (1995).

[31] P. Lambropoulos and D. Petrosyan, *Fundamentals of Quantum Optics and Quantum Information* (Springer, New York, 2007).

[32] N. Åibalić, J. Pritchard, C. Adams, and K. Weatherill, ARC: An open-source library for calculating properties of alkali Rydberg atoms, Comput. Phys. Commun. **220**, 319 (2017).

[33] I. I. Beterov, I. I. Ryabtsev, D. B. Tretyakov, and V. M. Entin, Quasiclassical calculations of blackbody-radiation-induced depopulation rates and effective lifetimes of Rydberg *ns*, *np*, and *nd* alkali-metal atoms with $n \leqslant 80$, Phys. Rev. A **79**, 052504 (2009).

[34] D. Petrosyan, M. Höning, and M. Fleischhauer, Spatial correlations of Rydberg excitations in optically driven atomic ensembles, Phys. Rev. A **87**, 053414 (2013).

[35] M. Fleischhauer, A. Imamoglu, and J. P. Marangos, Electromagnetically induced transparency: Optics in coherent media, Rev. Mod. Phys. **77**, 633 (2005).

[36] K. Kumar, H. Duan, R. S. Hegde, S. C. W. Koh, J. N. Wei, and J. K. W. Yang, Printing colour at the optical diffraction limit, Nat. Nanotechnol. **7**, 557 (2012).

[37] Z. Wang, W. Guo, L. Li, B. Luk'Yanchuk, A. Khan, Z. Liu, Z. Chen, and M. Hong, Optical virtual imaging at 50 nm lateral resolution with a white-light nanoscope, Nat. Commun. **2**, 218 (2011).

[38] H. Bao, J. Duan, S. Jin, X. Lu, P. Li, W. Qu, M. Wang, I. Novikova, E. E. Mikhailov, K.-F. Zhao *et al.*, Spin squeezing of 10^{11} atoms by prediction and retrodiction measurements, Nature (London) **581**, 159 (2020).

[39] Q. Zhang, Z. Bai, and G. Huang, Fast-responding property of electromagnetically induced transparency in Rydberg atoms, Phys. Rev. A **97**, 043821 (2018).

[40] Y.-W. Guo, S.-L. Xu, J.-R. He, P. Deng, M. R. Belić, and Y. Zhao, Transient optical response of cold Rydberg atoms with electromagnetically induced transparency, Phys. Rev. A **101**, 023806 (2020).

[41] M. S. Robbins and B. J. Hadwen, The noise performance of electron multiplying charge-coupled devices, IEEE Trans. Electron Devices **50**, 1227 (2003).

[42] C. W. Gardiner, J. Ye, H. C. Nagerl, and H. J. Kimble, Evaluation of heating effects on atoms trapped in an optical trap, Phys. Rev. A **61**, 045801 (2000).

[43] D.-S. Ding, H. Busche, B.-S. Shi, G.-C. Guo, and C. S. Adams, Phase Diagram and Self-Organizing Dynamics in a Thermal Ensemble of Strongly Interacting Rydberg Atoms, Phys. Rev. X **10**, 021023 (2020).

[44] S. Helmrich, A. Arias, G. Lochead, T. M. Wintermantel, M. Buchhold, S. Diehl, and S. Whitlock, Signatures of self-organized criticality in an ultracold atomic gas, Nature (London) **577**, 481 (2020).

[45] M. G. L. Gustafsson, Surpassing the lateral resolution limit by a factor of two using structured illumination microscopy. Short communication, J. Microsc. **198**, 82 (2000).

[46] M. J. Rust, M., Bates, and X. Zhuang, Sub-diffraction-limit imaging by stochastic optical reconstruction microscopy (STORM), Nat. Methods **3**, 793 (2006).

[47] A. Ghosh, D. J. Roth, L. H. Nicholls, W. P. Wardley, A. V. Zayats, and V. A. Podolskiy, Machine learning-based diffractive image analysis with subwavelength resolution, ACS Photonics **8**, 1448 (2021).

[48] Z.-M. Li, S.-B. Wu, J. Gao, H. Zhou, Z.-Q. Yan, R.-J. Ren, S.-Y. Yin, and X.-M. Jin, Fast correlated-photon imaging enhanced by deep learning, Optica **8**, 323 (2021).

[49] D. Petrosyan, Two-dimensional crystals of Rydberg excitations in a resonantly driven lattice gas, Phys. Rev. A **88**, 043431 (2013).

[50] M. Höning, D. Muth, D. Petrosyan, and M. Fleischhauer, Steady-state crystallization of Rydberg excitations in an optically driven lattice gas, Phys. Rev. A **87**, 023401 (2013).

[51] F. Cinti, P. Jain, M. Boninsegni, A. Micheli, P. Zoller, and G. Pupillo, Supersolid Droplet Crystal in a Dipole-Blockaded Gas, Phys. Rev. Lett. **105**, 135301 (2010).

[52] Y. Li, A. Geißler, W. Hofstetter, and W. Li, Supersolidity of lattice bosons immersed in strongly correlated Rydberg dressed atoms, Phys. Rev. A **97**, 023619 (2018).